Journal of Alloys and Compounds 780 (2019) 326–333

Contents lists available at ScienceDirect

Journal of Alloys and Compounds

journal homepage: http://www.elsevier.com/locate/jalcom

Nickel vanadate microspheres with numerous nanocavities synthesized by spray drying process as an anode material for Li-ion batteries

Jin-Sung Park [a], Jung Sang Cho [b], Yun Chan Kang [a, *]

[a] Department of Materials Science and Engineering, Korea University, Anam-Dong, Seongbuk-Gu, Seoul, 136-713, Republic of Korea
[b] Department of Engineering Chemistry, Chungbuk National University, Chungbuk, 361-763, Republic of Korea

ARTICLE INFO

Article history:
Received 24 April 2018
Received in revised form
10 October 2018
Accepted 21 November 2018
Available online 22 November 2018

Keywords:
Nanostructured materials
Nickel vanadate
Carbon composite
Spray drying
Lithium-ion battery

ABSTRACT

For use in next-generation energy storage applications, including electric vehicles, capacity and cycle life of lithium ion batteries need further improvement. Moreover, to achieve fast lithiation kinetics of the electrode materials, high power density and quick charging ability are necessary. Nickel vanadate ($Ni_3V_2O_8$) microsphere with tens of nanocavities is one of candidates for anode materials suitable for lithium ion batteries. The synthesis of microspheres is possible by a pilot-scale spray drying process and facile one-step oxidation heat treatment. Dextrin, which is present in the microspheres after spray drying process, plays a key role in the formation of nanocavities. Oxidation at different temperatures yields carbon composite microspheres with nanocavities and hierarchical $Ni_3V_2O_8$ microspheres with nanocavities. The nanocavities facilitate electrolyte contact with the electrode material and alleviate volume change during lithiation/delithiation. The merits of the nanocavities in the $Ni_3V_2O_8$ microspheres enable a high discharge capacity of 1045 mA h g^{-1} for the 2nd cycle at 1 A g^{-1} and long cycle life. Furthermore, $Ni_3V_2O_8$ microspheres deliver a high discharge capacity of 612 mA h g^{-1} at a high current density of 6 A g^{-1}.

1. Introduction

Lithium-ion batteries (LIBs) have been widely studied and are now utilitarian tools in our daily lives [1–6]. However, the battery performance must be further improved to meet the criteria of emerging applications such as electric vehicles and energy storage systems [7–9]. Therefore, the development of electrode materials with higher electrochemical performance to meet the impending demands for energy storage has continued to gain impetus [7–9]. The architectural design of nanostructured electrode materials is considered one of the fundamental approaches for achieving enhanced electrochemical properties [10–15]. The merits of nanostructured materials include large contact area with the electrolyte, short Li^+ ion and electron pathway, and buffering of volume expansion during the lithiation/delithiation processes [16,17]. Furthermore, properly designed materials offer active sites that provide capacitive behavior, which enables fast lithiation kinetics [18,19].

Introduction of hollow voids within the nanostructures has been proven effective for enhancing the electrochemical performance of electrode materials [20–25]. Ying et al. fabricated Sn nanodots embedded inside N-doped carbon microcages as anode materials for high-performance lithium- and sodium-ion batteries [24]. The structural stress exerted on the Sn nanodots during the electrochemical reaction was alleviated by the void spaces within the microsphere. Choi et al. synthesized 3D MoS_2-graphene microspheres consisting of multiple nanospheres for effective sodium ion storage [25]. The void spaces resulted in enhanced cycle performance of the MoS_2-graphene material for up to 600 cycles at a current density of 1.5 A g^{-1}, with a capacity retention of 84%. The rate performance was also improved compared to that of MoS_2-graphene without voids. Along with the structural merits, selecting an adequate composition for electrode materials can augment the battery performance [26–28]. The methods for synthesis of nanostructured materials are commonly based on liquid solution processes that are time consuming and pose challenges in terms of maintaining the homogeneity when scaled up [29,30]. On the other hand, the spray drying method, a type of gas-phase synthesis, is

* Corresponding author.
E-mail address: yckang@korea.ac.kr (Y. Chan Kang).

https://doi.org/10.1016/j.jallcom.2018.11.291
0925-8388/

used in the preparation of microspheres with a relatively uniform size [31–35]. Nickel vanadate ($Ni_3V_2O_8$) material has recently received much research attention and studied for use as anode in LIBs [36–39]. Lu et al. demonstrated a facile self-templating strategy for the synthesis of metal vanadate nanomaterials with complex chemical composition of $NiCo_2V_2O_8$ and a unique yolk–double shell structure showing excellent lithium-ion storage performances [37]. The characteristics of the transition metal oxide materials as anode materials for LIBs could be affected by their preparation processes. However, the synthesis of nanostructured transition metal vanadate electrode materials via a facile spray process has not been reported.

In this study, the spray drying method is used to synthesize two types of metal vanadate microspheres with nanocavities. By exploiting the segregation characteristics of the metal salt and dextrin, $Ni_3V_2O_8$-carbon composite microspheres and hierarchical $Ni_3V_2O_8$ microspheres consisting of nanorods are synthesized via a spray drying process and facile one-step heat treatment in air. During the spray drying process, the phase-segregated dextrin is decomposed and combusted, leaving empty nanocavities in the microspheres. The electrochemical properties of the transition metal vanadate microspheres with empty nanocavities are compared with those of transition metal vanadate microspheres without voids, prepared via spray drying from a solution without dextrin.

2. Experimental section

2.1. Sample preparation

$Ni_3V_2O_8$ microspheres with numerous nanocavities were prepared via spray drying and one-step heat treatment in air atmosphere. Firstly, dense spherical microspheres were synthesized via spray drying using an aqueous solution containing 0.075 M ammonium vanadate (98%, Samchun Chemicals), 0.075 M $Ni(NO_3)_2 \cdot H_2O$ (98%, Sigma Aldrich), and 40 g L^{-1} of dextrin [$(C_6H_{10}O_5)_n$, Samchun Chemicals]. Ammonium vanadate was firstly put into 500 mL of distilled water and the solution was vigorously stirred for 2 h at 90 °C. The other chemical reagents were subsequently added and dissolved without difficulty. The greenish transparent solution was drawn to a two-fluid nozzle and then atomized at 2.0 bar. The inlet and outlet temperatures of the spray dryer were set to 300 and 120 °C, respectively. The spray-dried powders were placed on an alumina boat and placed into a furnace. The heat treatment temperatures of the powders were 300 and 650 °C and the temperature was ramped at a rate of 10 °C min^{-1} under air atmosphere.

2.2. Characterization techniques

The morphologies of the $Ni_3V_2O_8$ microspheres were characterized via microscopic techniques, i.e., field emission transmission electron microscopy (FE-TEM; JEOL, JEM-2100F) and field emission scanning electron microscopy (FE-SEM). In order to elucidate the chemical nature of the species, X-ray photoelectron spectroscopy (XPS; Thermo Scientific K-Alpha) with focused monochromatic Al-K_α radiation at 12 kV and 20 mA was adopted. The crystallographic properties of the microspheres were analyzed via X-ray diffraction (XRD; X'Pert PRO MPD) using Cu-K_α radiation ($\lambda = 1.5418$ Å). Thermogravimetric analysis (TGA) was carried out with a Pyris 1 TGA (Perkin Elmer, temperature range = 25–600 °C, heating rate = 10 °C min^{-1}) instrument at the Korea Basic Science Institute (Pusan). The surface areas and the porosity properties were analyzed via the Brunauer–Emmett–Teller (BET) method using N_2 as the adsorbate gas. The structure of carbon in the microspheres was analyzed by Raman spectroscopy (Jobin Yvon LabRam, HR800, excitation source = 632.8 nm He–Ne laser) at room temperature.

2.3. Electrochemical measurements

Coin cells (2032-type) were assembled to analyze the electrochemical properties of the $Ni_3V_2O_8$ microspheres. The active material, carbon black, and sodium carboxymethyl cellulose (CMC) were mixed in a weight ratio of 7:2:1 using a mortar in order to prepare the anode material. Lithium metal and polypropylene film were adopted as the counter electrode and separator, respectively. The electrolyte used in this study was fluoroethylene carbonate/dimethyl carbonate (FEC/DMC; 1:1 v/v) containing 1 M $LiPF_6$. The discharge/charge characteristics of the $Ni_3V_2O_8$ microspheres at various current densities were analyzed in the potential range of 0.001–3 V. Cyclic voltammograms were acquired in the same potential range at respective scan rates of 0.1, 0.5, 1.0, and 2.0 mV s^{-1}. The diameter of the negative electrode containing the active material was 1.4 cm, with an approximate mass loading of 1.1 mg cm^{-2}. The Nyquist plots of the microspheres were analyzed over the frequency range of 0.01 Hz–100 kHz via electrochemical impedance spectroscopy (EIS).

3. Results and discussion

The formation mechanism of the $Ni_3V_2O_8$ microspheres comprising tens of nanocavities, prepared via the pilot-scale spray drying process and subsequent one step oxidation process, is illustrated in Scheme 1. Droplets atomized from the two-fluid nozzle were subjected to spray drying process and dense microspheres containing nickel nitrate, ammonium vanadate, and dextrin were produced, as shown in the SEM image in Fig. S1. Subsequently, the dried powders were subjected to one-step heat treatment in air at 300 and 650 °C and yielded $Ni_3V_2O_8$-C composite microspheres and hierarchical $Ni_3V_2O_8$ microspheres with rods, respectively. The two microspheres are hereinafter denoted as $Ni_3V_2O_8$/C-300 and H-$Ni_3V_2O_8$-650, respectively. The microspheres with nanocavities were formed from the oxidation of nickel nitrate and ammonium vanadate, and the combustion of phase-segregated dextrin at high temperature. To investigate the formation mechanism of the microspheres with nanocavities, a solution containing ammonium vanadate and dextrin was spray dried and calcined in air at 300 °C. The SEM images of the spray dried ammonium vanadate and dextrin, and the calcined V_2O_5 microspheres are shown in Figs. S2a and S2b, respectively. A dense structure was generated after calcination because the vanadium component was not phase-segregated from dextrin. The nickel component, which phase segregates from dextrin, formed a solid solution with the vanadium component during heat treatment, and microspheres with nanocavities were formed via the combustion of dextrin.

The morphologies of $Ni_3V_2O_8$/C-300 microspheres obtained by post-treatment of the spray-dried microspheres at a low temperature of 300 °C are shown in Fig. 1. The SEM and TEM images of $Ni_3V_2O_8$/C-300 microspheres in Fig. 1a–d reveal non-aggregated spherical microspheres containing tens of nanocavities. The fractured microsphere in the inset SEM image in Fig. 1a clearly shows the nanocavities distributed throughout the microsphere. The close-up SEM image of broken $Ni_3V_2O_8$/C-300 microsphere that shows inner structure can be seen in Fig. S3a. Fig. 1d shows a close-up TEM image of $Ni_3V_2O_8$/C-300 microsphere; the $Ni_3V_2O_8$-carbon composite framework and nanocavities could be well observed. The ultrafine $Ni_3V_2O_8$ nanocrystals observed in the TEM image could be attributed to the amorphous carbon matrix that restricted growth of the nanocrystals. Fig. 1e shows a high-resolution TEM image of the $Ni_3V_2O_8$ microsphere with lattice fringes separated by 2.30 Å

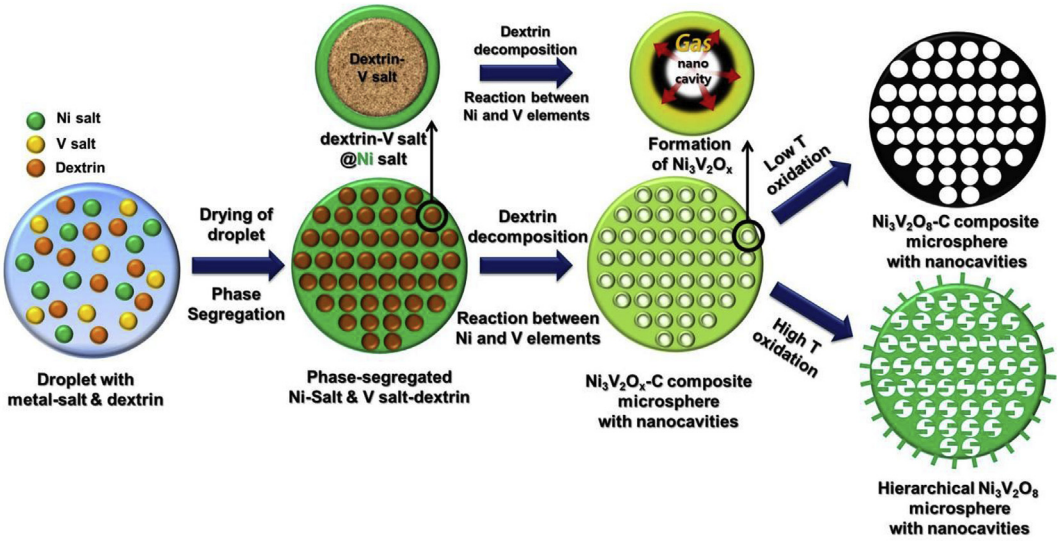

Scheme 1. Formation mechanism of $Ni_3V_2O_8$ microspheres with numerous nanocavities.

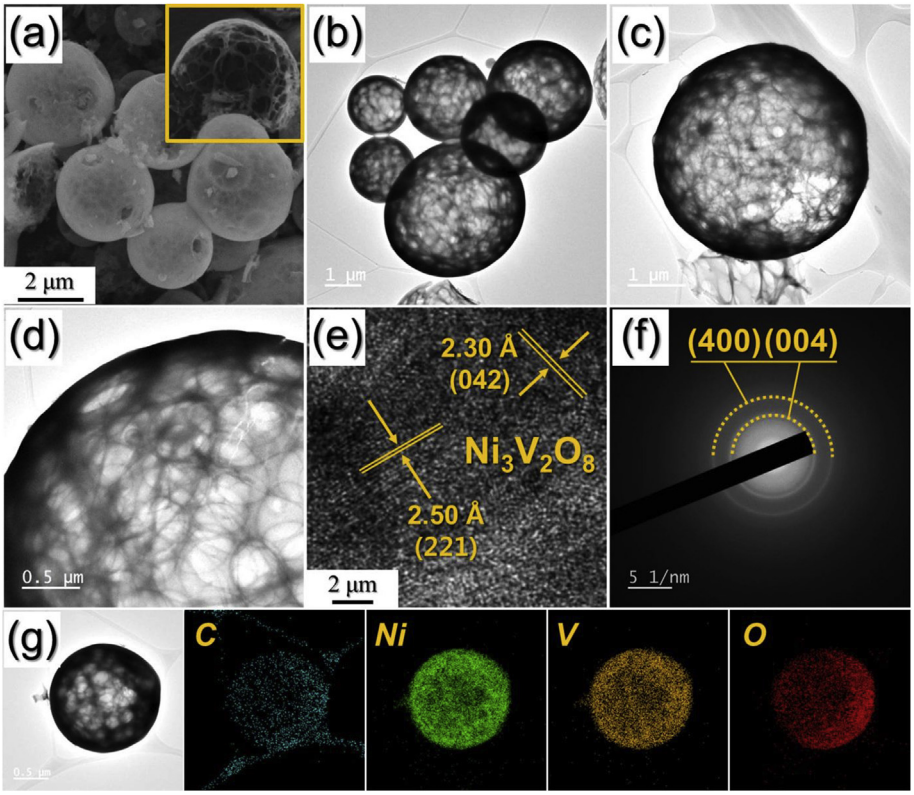

Fig. 1. Morphologies, SAED pattern, and elemental mapping images of $Ni_3V_2O_8$-carbon ($Ni_3V_2O_8$/C-300) composite microspheres with nanocavities: (a) SEM image, (b–d) TEM images, (e) HR-TEM image, (f) SAED pattern, and (g) elemental mapping images.

and 2.50 Å, corresponding to the (042) and (221) planes of the $Ni_3V_2O_8$ phase (JCPDS card #70–1394), respectively. The crystal structure of $Ni_3V_2O_8$/C-300 microspheres was further evaluated from the selected area electron diffraction (SAED) pattern shown in Fig. 1f. The diffraction rings correspond to the (004) and (400) planes of the $Ni_3V_2O_8$ phase. The elemental dot mapping images of $Ni_3V_2O_8$/C-300 microsphere shown in Fig. 1g reveal the uniform distribution of C, Ni, V, and O throughout the microsphere. The oxidation temperature of 300 °C was not high enough for the combustion of carbon in the microsphere. Raman spectrum of $Ni_3V_2O_8$/C composite microspheres in Fig. S4 showed broad peaks at 1360 cm^{-1} and 1590 cm^{-1}, which correspond to the D and G bands of carbon, respectively. The degree of graphitization for carbon material can be obtained by dividing the peak intensity of the D-band (I_D) by that of G-band (I_G). The calculated I_D/I_G ratio (= 0.84) revealed that carbon is highly disordered, which infers the porous nature of carbon [40].

The morphology, SAED pattern, and elemental mapping images

of H-$Ni_3V_2O_8$-650 microsphere post-treated at 650 °C are shown in Fig. 2. The SEM image shown in Fig. 2a reveals spherical particles consisting of hierarchical nanorods. The inset SEM image further reveals the interior of the microsphere; nanorods constituting the microspheres could be well observed. The magnified SEM image of broken H-$Ni_3V_2O_8$-650 microsphere is shown in Fig. S3b. Growth of the $Ni_3V_2O_8$ crystals occurred in the preferential crystallographic direction, forming $Ni_3V_2O_8$ nanorods. The $Ni_3V_2O_8$ nanorods were randomly anchored on the $Ni_3V_2O_8$ framework, resulting in hierarchical $Ni_3V_2O_8$ microspheres. The TEM images shown in Fig. 2b–d further clarify the internal structure of the synthesized microsphere. Fig. 2b and c reveal the nanocavities constituting the $Ni_3V_2O_8$ microspheres. When compared with Fig. 1d, the TEM image in Fig. 2d reveals larger $Ni_3V_2O_8$ nanocrystals with a rod-like shape, formed at higher oxidation temperature. Carbon combustion also played a role in formation of the larger nanocrystals. Fig. 2e reveals a lattice fringe with a spacing of 2.86 Å, corresponding to the (040) plane of $Ni_3V_2O_8$ (JCPDS card #70–1394). The SAED pattern in Fig. 2f provides further information on the crystal structure of the $Ni_3V_2O_8$ microspheres. The d-spacing values of 2.99, 2.63, and 2.22 Å correspond to the (131), (220), and (222) planes.

The elemental dot mapping images shown in Fig. 2g reveal the uniform distribution of Ni, V, and O within the microspheres. Carbon was not detected due to the high post-treatment temperature.

The chemical states of nickel, vanadium, and oxygen in H-$Ni_3V_2O_8$-650 microspheres with numerous nanocavities were examined by X-ray photoelectron spectroscopy (XPS). The Ni 2p spectrum shown in Fig. 3a revealed two major peaks corresponding to Ni $2p_{3/2}$ and Ni $2p_{1/2}$ doublets and satellite peaks. The Ni $2p_{3/2}$ peak was divided into two peaks at 856.2 and 858.0 eV, characteristic of Ni^{2+} and Ni^{3+}, respectively [41,42]. Likewise, the Ni $2p_{1/2}$ peak was deconvoluted into two peaks at 873.7 and 880.2 eV, corresponding to Ni^{2+} and Ni^{3+}, respectively [41,42]. The other peaks were satellite peaks, which is in accordance with the Ni 2p spectra reported in previous studies [41–43]. The V 2p spectrum in Fig. 3b shows peaks at binding energies of 516.7/523.6 eV and 517.3/524.7 eV, corresponding to the $2p_{3/2}$ and $2p_{1/2}$ states of the V^{4+}/V^{3+} species, respectively [38,39]. Two peaks were observed in the O 1s spectrum (Fig. 3c). The fitted peak at 530.7 eV is attributed to the typical metal-oxygen bonding in the $Ni_3V_2O_8$ microspheres [44,45]. The other peak at 532.8 eV is associated with oxygen deficient regions within the $Ni_3V_2O_8$ material [44,45].

The morphology of the microspheres containing the Ni and V salts, prepared from a solution without dextrin under spray drying conditions identical to those used for the microspheres with numerous nanocavities, is shown in Fig. S5a. Phase segregation did not occur for the microspheres that did not contain dextrin. Oxidation of the spray-dried powders without dextrin resulted in dense-structured $Ni_3V_2O_8$ microspheres, as shown in Fig. S5b. The phase and crystal structures of the prepared microspheres were analyzed by X-ray powder diffraction, as shown in Fig. 4. The SEM image of broken microsphere in Fig. S3c clearly reveals the formation of dense structured microsphere. The peaks of $Ni_3V_2O_8$/C-300, H-$Ni_3V_2O_8$-650, and dense $Ni_3V_2O_8$ microspheres were in accordance with those of the $Ni_3V_2O_8$ phase.

Thermogravimetric analysis (TGA) was used to calculate the amount of carbon in $Ni_3V_2O_8$/C-300 and H-$Ni_3V_2O_8$-650 microspheres. Two-step weight loss was observed in the TG curve of $Ni_3V_2O_8$/C-300 microspheres shown in Fig. S6a. Firstly, the weight loss below 200 °C is attributed to the evaporation of water molecules adsorbed in the microsphere. The abrupt weight loss between 420 and 480 °C is attributed to the combustion of amorphous carbon. The amount of carbon in $Ni_3V_2O_8$/C-300 microspheres,

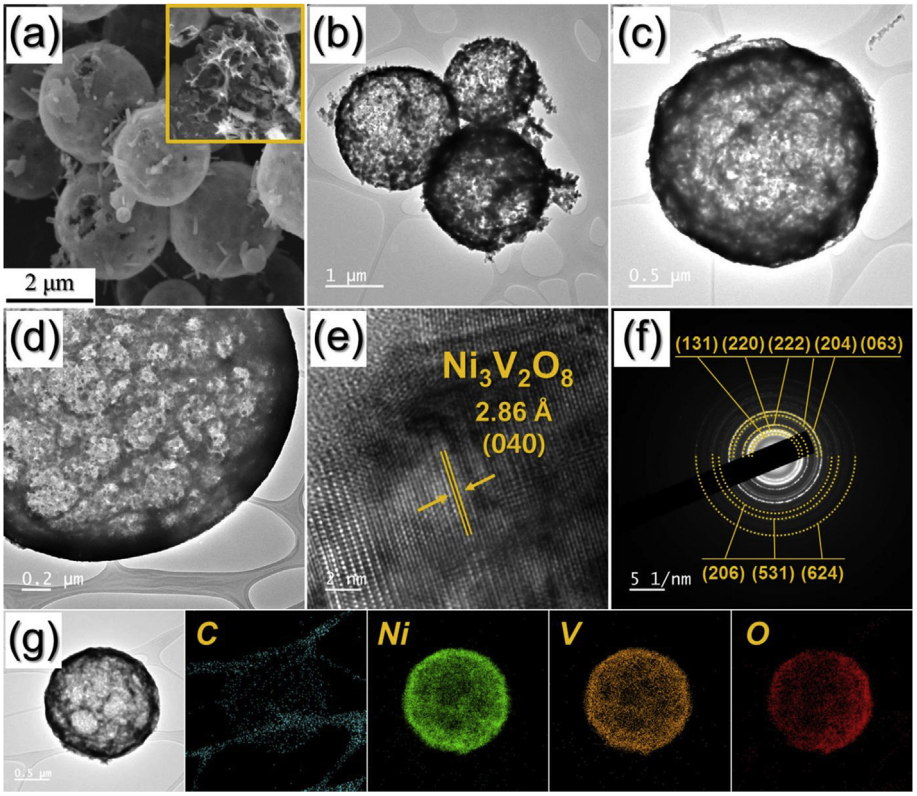

Fig. 2. Morphologies, SAED, and elemental mapping images of hierarchical $Ni_3V_2O_8$ H-($Ni_3V_2O_8$-650) microspheres with nanocavities: (a) SEM image, (b–d) TEM images, (e) HR-TEM image, (f) SAED pattern, and (g) elemental mapping images.

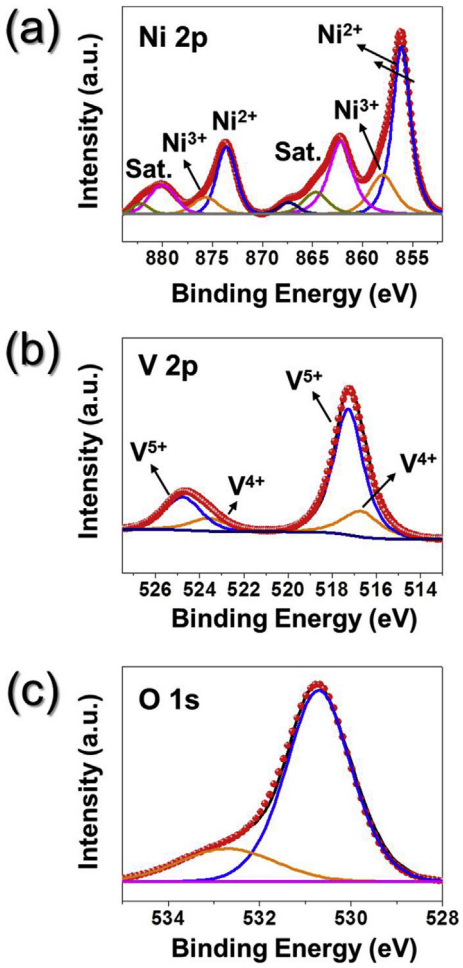

Fig. 3. XPS spectra of H-$Ni_3V_2O_8$-650 microspheres with nanocavities: (a) Ni 2p, (b) V 2p, and (c) O 1s.

determined by TG, was 7.6 wt%. The TG curve of H-$Ni_3V_2O_8$-650 microspheres presented in Fig. S6b did not show any weight change, confirming the elimination of amorphous carbon during the oxidation step. The TGA curve of dense $Ni_3V_2O_8$ microspheres in air shown in Fig. S6c didn't show weight fluctuation. It is due to the lack of carbon material and formation of $Ni_3V_2O_8$ nanocrystals at a high oxidation temperature.

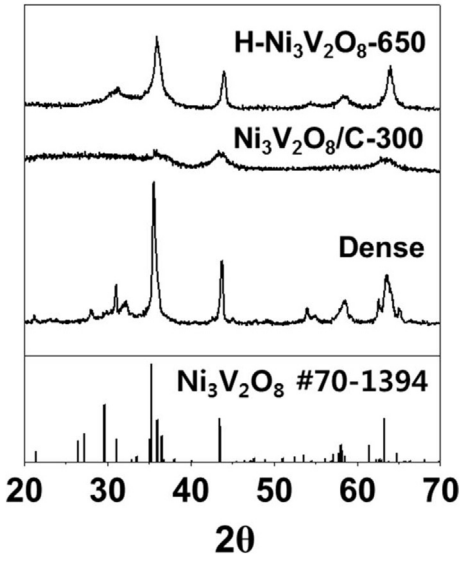

Fig. 4. XRD patterns of $Ni_3V_2O_8$/C-300, H-$Ni_3V_2O_8$-650, and dense $Ni_3V_2O_8$ microspheres.

The porosity of the uniquely structured microspheres with tens of nanocavities was analyzed by the BET method. The specific surface areas of $Ni_3V_2O_8$/C-300 and H-$Ni_3V_2O_8$-650 microspheres and dense $Ni_3V_2O_8$ microspheres were 15, 24, and 4 $m^2 g^{-1}$, respectively, as shown in Fig. S7a. H-$Ni_3V_2O_8$-650 microspheres exhibited the highest specific surface area due to combustion of the amorphous carbon. The specific surface area of the dense $Ni_3V_2O_8$ microspheres was the lowest, presumably due to crystal growth at the high oxidation temperature. The N_2 sorption isotherms shown in Fig. S7a verified that the microspheres with nanocavities consisted of mesopores. The most frequently occurring pore size in the BJH pore size distribution shown in Fig. S7b was over 20 nm.

The electrochemical properties of the $Ni_3V_2O_8$ microspheres are presented in Fig. 5–7. Cyclic voltammograms (CVs) of H-$Ni_3V_2O_8$-650 microspheres were acquired at different sweep rates over the potential range of 0.001–3 V (vs. Li/Li^+), as shown in Fig. 5a. H-$Ni_3V_2O_8$-650 microspheres obeyed the power law relationship, $i = av^b$, where a is a constant and b can vary from 0.5 to 1.0. As the b-value approaches unity, reaction is mostly from surface capacitive effect [18,46–48]. Fig. 5b shows the log(peak current) vs. log(sweep rate) curves corresponding to peak 1 and peak 2. The calculated b-values for peak 1 and peak 2 were 0.88 and 0.94, respectively, which indicates that the electrochemical reaction of the H-$Ni_3V_2O_8$-650 microspheres was mainly derived from the capacitive process. In order to gain further insight into the capacity contribution, the total stored charge in the electrode material was separated into capacitive and diffusion-limited elements. Furthermore, the capacitive contribution can be quantitatively distinguished using the follow equation:

$$i = k_1 v + k_2 v^{1/2}$$

At a fixed potential, the current is determined from the capacitive effects ($k_1 v$) and diffusion-limited process ($k_2 v^{1/2}$) [18,46,47]. By plotting $i/v^{1/2}$ vs. $v^{1/2}$, the k_1 and k_2 values can be obtained from the linear profile; k_1 and k_2 correspond to the slope and the y-axis intercept, respectively. From comparison of the shaded area ($k_1 v$) with the experimentally obtained current curves, about 92% of the total current of H-$Ni_3V_2O_8$-650 microspheres was derived from the capacitive element at a sweep rate of 1.0 mV s^{-1}, which is in accordance with the b-value that was close to unity. The capacitive contributions to the capacity at various sweep rates are shown in Fig. 5d. The capacitive contribution increased from 74% to 94% when the sweep rate was increased from 0.1 to 2.0 mV s^{-1}. In order to understand the reduction/oxidation reactions that occur during cycling, the CV curves of $Ni_3V_2O_8$/C-300, H-$Ni_3V_2O_8$-650, and dense $Ni_3V_2O_8$ microspheres for the first five cycles were obtained at a fixed scan rate of 0.1 mV s^{-1}. Several electrochemical reactions were observed in the CV curves as shown in Fig. S8. During the first discharge process, $Ni_3V_2O_8$ material was primarily transformed into NiO accompanied by $Li_xV_2O_5$ formation [36,49]. In addition, peaks corresponding to further insertion of lithium ions into $Li_xV_2O_5$ (where $Li_{x+y}V_2O_5$ is formed as the product) and reduction of Ni^{2+} to Ni metal were observed [36,49]. Two anodic peaks at 1.3 and 2.5 V correspond to oxidation of Ni to Ni^{2+} and extraction of lithium ion from $Li_{x+y}V_2O_5$ matrix [36,49]. From the second cycle and on, peaks corresponding to reversible conversion reaction of NiO and intercalation reaction of $Li_xV_2O_5$ were observed [36,49].

The initial charge/discharge profiles of the $Ni_3V_2O_8$

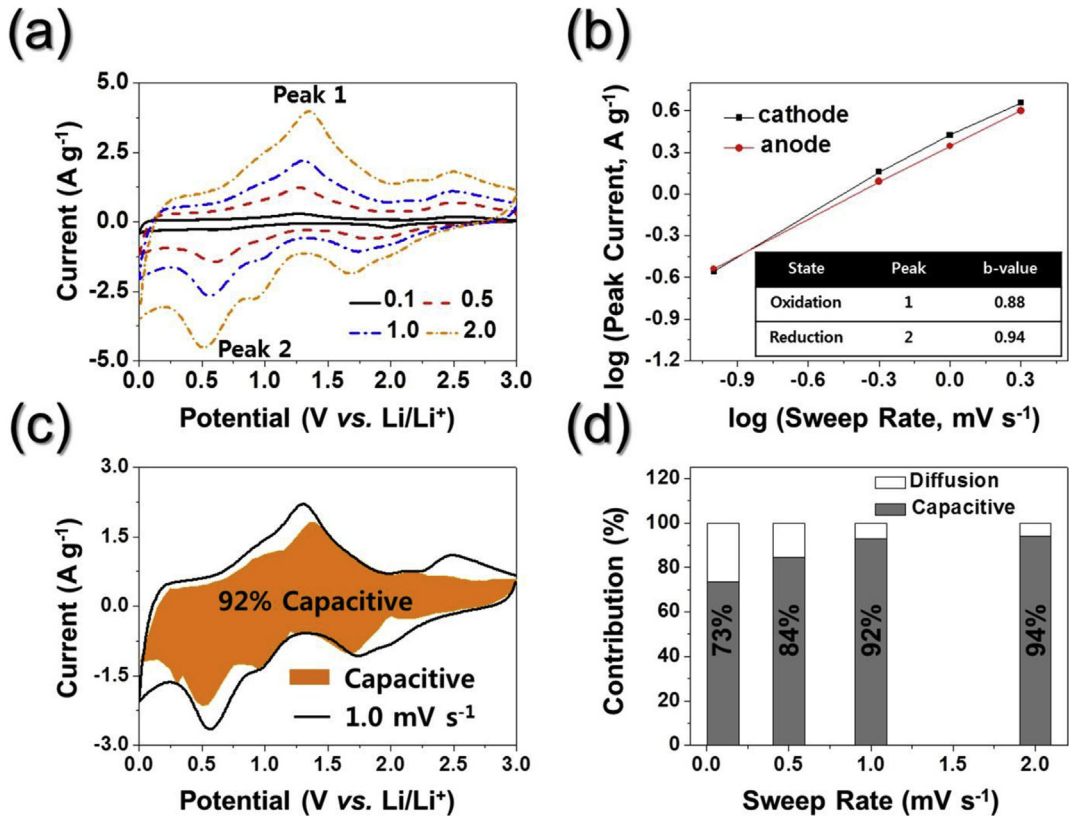

Fig. 5. a) Cyclic voltammograms of H-$Ni_3V_2O_8$-650 electrode at various sweep rates, b) Fitted ln(peak current) vs. ln(scan rate) for Peak 1 and Peak 2, c) cyclic voltammogram showing capacitive contribution (colored area) to the total current, d) capacity contribution at different scan rates.

microspheres shown in Fig. 6a were consistent with the CV data. Anodic plateaus were observed at 1.3 and 2.5 V, related to the oxidation of Ni to NiO and lithium ion extraction from $Li_{x+y}V_2O_5$ [36,49]. Initial discharge capacities of 1349, 1280, and 1120 mA h g^{-1} at a current density of 1 A g^{-1} were observed for $Ni_3V_2O_8$/C-300, H-$Ni_3V_2O_8$-650, and dense $Ni_3V_2O_8$ microspheres, respectively, and the corresponding Coulombic efficiencies were 75, 83, and 84%, respectively. $Ni_3V_2O_8$/C-300 microspheres showed the lowest initial coulombic efficiency owing to the presence of amorphous carbon [50,51]. The cycling and rate performances of the $Ni_3V_2O_8$ microspheres are presented in Fig. 6b and c, respectively. The discharge capacities of $Ni_3V_2O_8$/C-300, H-$Ni_3V_2O_8$-650, and dense $Ni_3V_2O_8$ microspheres after 150 cycles at a current density of 1 A g^{-1} were 754, 763, and 496 mA h g^{-1}, respectively. The $Ni_3V_2O_8$ microspheres with nanocavities showed superior cycling performance compared to that of the dense $Ni_3V_2O_8$ microspheres due to the hollow nanocavities within the microspheres that alleviated the volume expansion during cycling. The discharge capacities of $Ni_3V_2O_8$/C-300/H-$Ni_3V_2O_8$-650 microspheres at current densities of 0.5, 1.0, 2.0, 4.0, and 6.0 A g^{-1} were 901/1000, 793/861, 710/784, 621/678, and 557/612 mA h g^{-1}, respectively. The discharge capacity of the dense $Ni_3V_2O_8$ microspheres declined from 845 to 400 mA h g^{-1} when the current density was increased from 0.5 to 6.0 A g^{-1}. The nanocavities distributed within the microspheres were beneficial for electron and Li^+ ion transport during the lithiation/delithiation process, which enabled a high capacity at a high current density of 6 A g^{-1}.

The Nyquist plots of $Ni_3V_2O_8$/C-300, H-$Ni_3V_2O_8$-650, and dense $Ni_3V_2O_8$ microspheres before cycling and after the 1st, 10th, and 50th cycles are shown in Fig. 7. The plots were obtained by using the Randle-type equivalent-circuit model. The charge transfer resistance (R_{ct}) could be obtained from the depressed semicircle in the

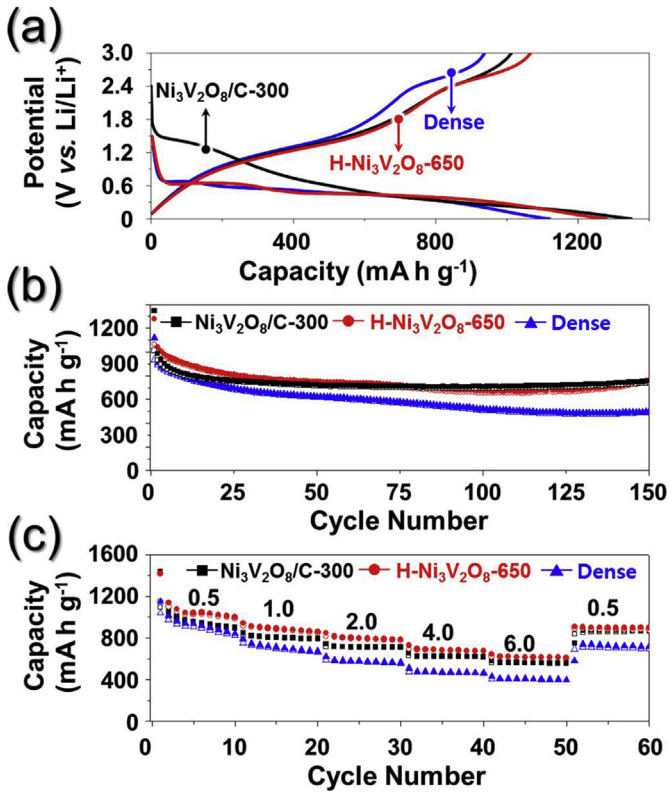

Fig. 6. Electrochemical properties of the microspheres with nanocavities and dense microspheres: (a) first charge-discharge curves, (b) cycling performances at a current density of 1 A g^{-1}, and (c) rate performances.

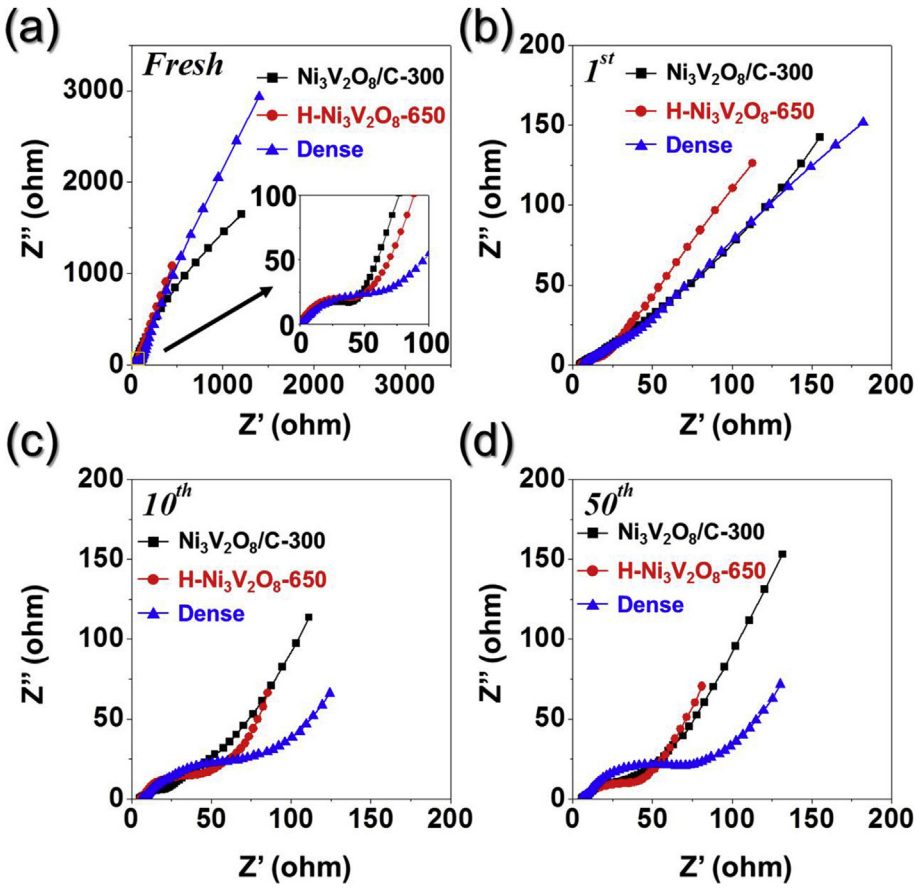

Fig. 7. Nyquist plots of $Ni_3V_2O_8$ microspheres (a) before cycling and after the (b) 1st, (c) 10th, and (d) 50th cycles.

medium-frequency region [52–55]. The R_{ct} values of $Ni_3V_2O_8$/C-300, H-$Ni_3V_2O_8$-650, and dense $Ni_3V_2O_8$ microspheres before cycling were 54, 63, and 82 Ω, respectively. $Ni_3V_2O_8$/C-300 microspheres with ultrafine $Ni_3V_2O_8$ nanocrystals showed the lowest R_{ct} value. H-$Ni_3V_2O_8$-650 exhibited a lower R_{ct} than the dense $Ni_3V_2O_8$ microspheres due to the nanocavities that accelerated the electron and Li^+ ion transfer kinetics. The R_{ct} values of all samples decreased abruptly after the 1st cycle due to the formation of ultrafine nanocrystals. $Ni_3V_2O_8$/C-300 and H-$Ni_3V_2O_8$-650 microspheres exhibited lower R_{ct} values during cycling compared to that of the dense $Ni_3V_2O_8$ microspheres, which verified the improved kinetics and structural stability of the microspheres containing numerous nanocavities. H-$Ni_3V_2O_8$-650 microspheres exhibited R_{ct} values of 20, 52, and 53 Ω after the 1st, 10th, and 50th cycles, respectively. To prove the structural stability of the microspheres, SEM images of $Ni_3V_2O_8$/C-300, H-$Ni_3V_2O_8$-650, and dense $Ni_3V_2O_8$ microspheres after 100 cycles at a current density of 1 A g^{-1} were obtained as shown in Fig. S9. The morphology of $Ni_3V_2O_8$/C-300 and H-$Ni_3V_2O_8$-650 microspheres was well maintained, whereas the dense $Ni_3V_2O_8$ microspheres disintegrated after cycling.

4. Conclusions

Using a simple spray drying process and calcination step, nickel vanadate microspheres with nanocavities were successfully synthesized and applied as the anode material for lithium-ion batteries. The pilot-scale spray drying process yielded microspheres consisting of phase-segregated dextrin that was later transformed into nanocavities, and metal salts. After simple oxidation in air, numerous nanocavities were generated in the $Ni_3V_2O_8$ microspheres. The structural merits of the synthesized microspheres enabled excellent electrochemical performance for lithium-ion storage. The effect of the nanocavities was confirmed by comparing the performance of batteries employing the $Ni_3V_2O_8$ microspheres with and without nanocavities. The two types of $Ni_3V_2O_8$ microspheres with nanocavities, i.e., with carbon and without, exhibited superior cycling and rate performance compared to the dense $Ni_3V_2O_8$ microspheres. The strategy demonstrated in this work may be applied to the preparation of metal oxide microspheres with nanocavities and can be tailored for use in various applications.

Acknowledgements

This work was supported by the National Research Foundation of Korea(NRF) grant funded by the Korea government(MSIP) (NRF-2017R1A2B2008592 and NRF-2017R1A4A1014806).

Appendix A. Supplementary data

Supplementary data to this article can be found online at https://doi.org/10.1016/j.jallcom.2018.11.291.

References

[1] B. Long, M.S. Balogun, L. Luo, Y. Luo, W. Qiu, S. Song, L. Zhang, Y. Tong, Encapsulated vanadium-based hybrids in amorphous N-doped carbon matrix as anode materials for lithium-ion batteries, Small 13 (2017) 1702081.
[2] M.S. Balogun, Y. Zeng, W. Qiu, Y. Luo, A. Onasanya, T.K. Olaniyi, Y. Tong, Three-dimensional nickel nitride (Ni_3N) nanosheets: free standing and flexible electrodes for lithium ion batteries and supercapacitors, J. Mater. Chem. 4

(2016) 9844–9849.
[3] Y. Lu, L. Yu, M. Wu, Y. Wang, X.W. Lou, Construction of complex Co_3O_4@$Co_3V_2O_8$ hollow structures from metal–organic frameworks with enhanced lithium storage properties, Adv. Mater. 30 (2018) 1702875.
[4] X. Zhou, L.J. Wan, Y.G. Guo, Binding SnO_2 nanocrystals in nitrogen-doped graphene sheets as anode materials for lithium-ion batteries, Adv. Mater. 25 (2013) 2152–2157.
[5] L. Shen, L. Yu, X.Y. Yu, X. Zhang, X.W.D. Lou, Self-templated formation of uniform $NiCo_2O_4$ hollow spheres with complex interior structures for lithium-ion batteries and supercapacitors, Angew. Chem. Int. Ed. 54 (2015) 1868–1872.
[6] B. Sambandam, V. Soundharrajan, J. Song, S. Kim, J. Jo, D.T. Pham, S. Kim, V. Mathew, K.H. Kim, Y.K. Sun, J. Kim, $Ni_3V_2O_8$ nanoparticles as an excellent anode material for high-energy lithium-ion batteries, J. Electroanal. Chem. 810 (2018) 34–40.
[7] S.K. Park, S.H. Yu, N. Pinna, S. Woo, B. Jang, Y.H. Chung, Y.H. Cho, Y.E. Sung, Y. Piao, A facile hydrazine-assisted hydrothermal method for the deposition of monodisperse SnO_2 nanoparticles onto graphene for lithium ion batteries, J. Mater. Chem. 22 (2012) 2520–2525.
[8] L. Yu, J.F. Yang, X.W.D. Lou, Formation of CoS_2 nanobubble hollow prisms for highly reversible lithium storage, Angew. Chem. Int. Ed. 55 (2016) 13422–13426.
[9] X. Zhou, L.J. Wan, Y.G. Guo, Binding SnO_2 nanocrystals in nitrogen-doped graphene sheets as anode materials for lithium-ion batteries, Adv. Mater. 25 (2013) 2152–2157.
[10] S.K. Park, J.S. Park, Y.C. Kang, Selenium-infiltrated metal–organic framework-derived porous carbon nanofibers comprising interconnected bimodal pores for Li–Se batteries with high capacity and rate performance, J. Mater. Chem. 6 (2018) 1028–1036.
[11] J.S. Park, S.Y. Jeong, K.M. Jeon, Y.C. Kang, J.S. Cho, Iron diselenide combined with hollow graphitic carbon nanospheres as a high-performance anode material for sodium-ion batteries, Chem. Eng. J. 339 (2018) 97–107.
[12] A. Pan, H.B. Wu, X.W. Lou, Template-free synthesis of VO_2 hollow microspheres with various interiors and their conversion into V_2O_5 for lithium-ion batteries, Angew. Chem. Int. Ed. 52 (2013) 2226–2230.
[13] J.S. Cho, J.S. Park, Y.C. Kang, Preparation of hollow Fe_2O_3 nanorods and nanospheres by nanoscale Kirkendall diffusion, and their electrochemical properties for use in lithium-ion batteries, Sci. Rep. 6 (2016) 38933.
[14] S.K. Park, J.K. Kim, Y.C. Kang, Electrochemical properties of uniquely structured Fe_2O_3 and $FeSe_2$/graphitic-carbon microrods synthesized by applying a metal-organic framework, Chem. Eng. J. 334 (2018) 2440–2449.
[15] G.D. Park, J.K. Lee, Y.C. Kang, Design and synthesis of Janus-structured mutually doped SnO_2–Co_3O_4 hollow nanostructures as superior anode materials for lithium-ion batteries, J. Mater. Chem. 5 (2017) 25319–25327.
[16] W.Y. Li, L.N. Xu, J. Chen, Co_3O_4 nanomaterials in lithium-ion batteries and gas sensors, Adv. Funct. Mater. 15 (2005) 851–857.
[17] H. Zhang, X. Huang, O. Noonan, L. Zhou, C. Yu, Tailored yolk–shell Sn@C nanoboxes for high-performance lithium storage, Adv. Funct. Mater. 27 (2017) 1606023.
[18] R. Sun, S. Liu, Q. Wei, J. Sheng, S. Zhu, Q. An, L. Mai, Mesoporous NiS_2 nanospheres anode with pseudocapacitance for high-rate and long-life sodium-ion battery, Small 13 (2017) 1701744.
[19] Q. Wang, Z.H. Wen, J.H. Li, A hybrid supercapacitor fabricated with a carbon nanotube cathode and a TiO_2–B nanowire anode, Adv. Funct. Mater. 16 (2006) 2141–2146.
[20] J.S. Park, Y.C. Kang, Multicomponent (Mo, Ni) metal sulfide and selenide microspheres with empty nanovoids as anode materials for Na-ion batteries, J. Mater. Chem. 5 (2017) 8616–8623.
[21] J.S. Xu, Y.J. Zhu, Monodisperse Fe_3O_4 and γ-Fe_2O_3 magnetic mesoporous microspheres as anode materials for lithium-ion batteries, ACS Appl. Mater. Interfaces 4 (2012) 4752–4757.
[22] Y.N. Ko, S.B. Park, Y.C. Kang, Design and fabrication of new nanostructured SnO_2-carbon composite microspheres for fast and stable lithium storage performance, Small 10 (2014) 3240–3245.
[23] J.S. Cho, J.M. Won, J.K. Lee, Y.C. Kang, Design and synthesis of multiroom-structured metal compounds–carbon hybrid microspheres as anode materials for rechargeable batteries, Nano Energy 26 (2016) 466–478.
[24] H. Ying, S. Zhang, Z. Meng, Z. Sun, W.Q. Han, Ultrasmall Sn nanodots embedded inside N-doped carbon microcages as high-performance lithium and sodium ion battery anodes, J. Mater. Chem. 5 (2017) 8334–8342.
[25] S.H. Choi, Y.N. Ko, J.K. Lee, Y.C. Kang, 3D MoS_2–graphene microspheres consisting of multiple nanospheres with superior sodium ion storage properties, Adv. Funct. Mater. 25 (2015) 1780–1788.
[26] Q. Wei, Q. Wang, Q. Li, Q. An, Y. Zhao, Z. Peng, Y. Jiang, S. Tan, M. Yan, L. Mai, Pseudocapacitive layered iron vanadate nanosheets cathode for ultrahigh-rate lithium ion storage, Nano Energy 47 (2018) 294–300.
[27] P. Liu, X. Xia, W. Lei, Q. Hao, Rational synthesis of highly uniform hollow core–shell Mn_3O_4/CuO@ TiO_2 submicroboxes for enhanced lithium storage performance, Chem. Eng. J. 316 (2017) 214–224.
[28] H. Zhao, Y. Li, Z. Zhu, J. Lin, Z. Tian, R. Wang, Structural and electrochemical characteristics of $Li_{4-x}Al_xTi_5O_{12}$ as anode material for lithium-ion batteries, Electrochim. Acta 53 (2008) 7079–7083.
[29] Z. Ju, E. Zhang, Y. Zhao, Z. Xing, Q. Zhuang, Y. Qiang, Y. Qian, One-pot hydrothermal synthesis of $FeMoO_4$ nanocubes as an anode material for lithium-ion batteries with excellent electrochemical performance, Small 11 (2015) 4753–4761.
[30] Y. Chen, B. Song, X. Tang, L. Lu, J. Xue, Ultrasmall Fe_3O_4 nanoparticle/MoS_2 nanosheet composites with superior performances for lithium ion batteries, Small 10 (2014) 1536–1543.
[31] G.W. Zhou, J. Wang, P. Gao, X. Yang, Y.S. He, X.Z. Liao, J. Yang, Z.F. Ma, Facile spray drying route for the three-dimensional graphene-encapsulated Fe_2O_3 nanoparticles for lithium ion battery anodes, Ind. Eng. Chem. Res. 52 (2013) 1197–1204.
[32] N. Tran, K.G. Bramnik, H. Hibst, J. Prölß, N. Mronga, M. Holzapfel, W. Scheifele, P. Novak, Spray-drying synthesis and electrochemical performance of lithium vanadates as positive electrode materials for lithium batteries, J. Electrochem. Soc. 155 (2008) A384–A389.
[33] B. Zou, Y. Wang, S. Zhou, Spray drying-assisted synthesis of $LiFePO_4$/C composite microspheres with high performance for lithium-ion batteries, Mater. Lett. 92 (2013) 300–303.
[34] D. Wang, M. Gao, H. Pan, Y. Liu, J. Wang, S. Li, H. Ge, Enhanced cycle stability of micro-sized Si/C anode material with low carbon content fabricated via spray drying and in situ carbonization, J. Alloy. Comp. 604 (2014) 130–136.
[35] D.S. Jung, T.H. Hwang, S.B. Park, J.W. Choi, Spray drying method for large-scale and high-performance silicon negative electrodes in Li-ion batteries, Nano Lett. 13 (2013) 2092–2097.
[36] Y. Li, L.B. Kong, M.C. Liu, W.B. Zhang, L. Kang, One-step synthesis of micro/nano flower-like $Ni_3V_2O_8$ as anode for Li-ion batteries, Mater. Lett. 186 (2017) 289–292.
[37] Y. Lu, J. Nai, X.W.D. Lou, Formation of $NiCo_2V_2O_8$ yolk–double shell spheres with enhanced lithium storage properties, Angew. Chem. 130 (2018) 2949–2953.
[38] C. Lv, J. Sun, G. Chen, C. Yan, D. Chen, Achieving $Ni_3V_2O_8$ amorphous wire encapsulated in crystalline tube nanostructure as anode materials for lithium ion batteries, Nano Energy 33 (2017) 138–145.
[39] V. Soundharrajan, B. Sambandam, J. Song, S. Kim, J. Jo, D.T. Pham, S. Kim, V. Mathew, J. Kim, Bitter gourd-shaped $Ni_3V_2O_8$ anode developed by a one-pot metal-organic framework-combustion technique for advanced Li-ion batteries, Ceram. Int. 43 (2017) 13224–13232.
[40] B. Kalimuthu, K. Nallathamby, Optimization of structure and porosity of nitrogen containing mesoporous carbon spheres for effective selenium confinement in futuristic lithium–selenium batteries, ACS Sustain. Chem. Eng. 6 (2018) 7064–7077.
[41] J.S. Cho, S.Y. Lee, H.S. Ju, Y.C. Kang, Synthesis of NiO nanofibers composed of hollow nanospheres with controlled sizes by the nanoscale Kirkendall diffusion process and their electrochemical properties, ACS Appl. Mater. Interfaces 7 (2015) 25641–25647.
[42] J.S. Cho, J.M. Won, J.-H. Lee, Y.C. Kang, Synthesis and electrochemical properties of spherical and hollow-structured NiO aggregates created by combining the Kirkendall effect and Ostwald ripening, Nanoscale 7 (2015) 19620–19626.
[43] E.E. Khawaja, M.A. Salim, M.A. Khan, F.F. Al-Adel, G.D. Khattak, Z. Hussain, XPS, auger, electrical and optical studies of vanadium phosphate glasses doped with nickel oxide, J. Non-Cryst. Solids 110 (1989) 33–43.
[44] P. Meduri, E. Clark, J.H. Kim, E. Dayalan, G.U. Sumanasekera, M.K. Sunkara, MoO_{3-x} nanowire arrays as stable and high-capacity anodes for lithium ion batteries, Nano Lett. 12 (2012) 1784–1788.
[45] N.N. Leyzerovich, K.G. Bramnik, T. Buhrmester, H. Ehrenberg, H. Fuess, Electrochemical intercalation of lithium in ternary metal molybdates $MMoO_4$ (M: Cu, Zn, Ni and Fe), J. Power Sources 127 (2004) 76–84.
[46] X. Deng, Z. Wei, C. Cui, Q. Liu, C. Wang, J. Ma, Oxygen-deficient anatase TiO_2@C nanospindles with pseudocapacitive contribution for enhancing lithium storage, J. Mater. Chem. 6 (2018) 4013–4022.
[47] V. Augustyn, J. Come, M.A. Lowe, J.W. Kim, P. L Taberna, S.H. Tolbert, H.D. Abruna, P. Simon, B. Dunn, High-rate electrochemical energy storage through Li^+ intercalation pseudocapacitance, Nat. Mater. 12 (2013) 518–522.
[48] S. Li, J. Qiu, C. Lai, M. Ling, H. Zhao, S. Zhang, Surface capacitive contributions: towards high rate anode materials for sodium ion batteries, Nano Energy 12 (2015) 224–230.
[49] Y. Li, L.B. Kong, M.C. Liu, L. Kang, Facile synthesis of a nickel vanadate/Ni composite and its electrochemical performance as an anode for lithium ion batteries, RSC Adv. 6 (2016) 90197–90205.
[50] S.H. Ng, J. Wang, D. Wexler, K. Konstantinov, Z.P. Guo, H.K. Liu, Highly reversible lithium storage in spheroidal carbon-coated silicon nanocomposites as anodes for lithium-ion batteries, Angew. Chem. Int. Ed. 45 (2006) 6896–6899.
[51] S.R. Mukai, T. Hasegawa, M. Takagi, H. Tamon, Reduction of irreversible capacities of amorphous carbon materials for lithium ion battery anodes by Li_2CO_3 addition, Carbon 42 (2004) 837–842.
[52] J.S. Cho, J.S. Park, Y.C. Kang, Porous FeS nanofibers with numerous nanovoids obtained by Kirkendall diffusion effect for use as anode materials for sodium-ion batteries, Nano Res 10 (2017) 897–907.
[53] J.S. Park, J.S. Cho, J.H. Kim, Y.J. Choi, Y.C. Kang, Electrochemical properties of micron-sized Co_3O_4 hollow powders consisting of size controlled hollow nanospheres, J. Alloy. Comp. 689 (2016) 554–563.
[54] S. Lu, T. Zhu, Z. Li, Y. Pang, L. Shi, S. Ding, G. Gao, Ordered mesoporous carbon supported $Ni_3V_2O_8$ composites for lithium-ion batteries with long-term and high-rate performance, J. Mater. Chem. 6 (2018) 7005–7013.
[55] K. Lee, S.Y. Shin, Y.S. Yoon, Fe_3O_4 nanoparticles on MWCNTs backbone for lithium ion batteries, J. Korean Ceram. Soc. 53 (2016) 376–380.